LETTER

doi:10.1038/nature23298

Large turbulent reservoirs of cold molecular gas around high-redshift starburst galaxies

E. Falgarone[1], M. A. Zwaan[2], B. Godard[1], E. Bergin[3], R. J. Ivison[2,4], P. M. Andreani[2], F. Bournaud[5], R. S. Bussmann[6], D. Elbaz[5], A. Omont[7], I. Oteo[2,4] & F. Walter[8]

Starburst galaxies at the peak of cosmic star formation[1] are among the most extreme star-forming engines in the Universe, producing stars over about 100 million years (ref. 2). The star-formation rates of these galaxies, which exceed 100 solar masses per year, require large reservoirs of cold molecular gas[3] to be delivered to their cores, despite strong feedback from stars or active galactic nuclei[4,5]. Consequently, starburst galaxies are ideal for studying the interplay between this feedback and the growth of a galaxy[6]. The methylidyne cation, CH^+, is a most useful molecule for such studies because it cannot form in cold gas without suprathermal energy input, so its presence indicates dissipation of mechanical energy[7–9] or strong ultraviolet irradiation[10,11]. Here we report the detection of CH^+ ($J=1$–0) emission and absorption lines in the spectra of six lensed starburst galaxies[12–15] at redshifts near 2.5. This line has such a high critical density for excitation that it is emitted only in very dense gas, and is absorbed in low-density gas[10]. We find that the CH^+ emission lines, which are broader than 1,000 kilometres per second, originate in dense shock waves powered by hot galactic winds. The CH^+ absorption lines reveal highly turbulent reservoirs of cool (about 100 kelvin), low-density gas, extending far (more than 10 kiloparsecs) outside the starburst galaxies (which have radii of less than 1 kiloparsec). We show that the galactic winds sustain turbulence in the 10-kiloparsec-scale environments of the galaxies, processing these environments into multiphase, gravitationally bound reservoirs. However, the mass outflow rates are found to be insufficient to balance the star-formation rates. Another mass input is therefore required for these reservoirs, which could be provided by ongoing mergers[16] or cold-stream accretion[17,18]. Our results suggest that galactic feedback, coupled jointly to turbulence and gravity, extends the starburst phase of a galaxy instead of quenching it.

Using the Atacama Large Millimeter Array (ALMA), we detected CH^+ ($J=1$–0) lines in high-redshift galaxies. Our sample (Table 1) consists of six particularly bright—by virtue of gravitational lensing—submillimetre-selected galaxies (SMGs), with specific star-formation rates that are more than about three times those of galaxies on the main sequence[19] at redshift $z\approx2$. The SMGs are extremely compact, with half-light radii (r_{SMG}) in the range 0.3–1.2 kpc inferred from lens modelling (Table 1). Their rest-frame 360-μm dust continuum images and CH^+ ($J=1-0$) spectra are displayed in Figs 1 and 2. Only the faintest target, SDP130, is not detected in absorption. The peak optical depths at the velocity resolution of 50 km s^{-1} are large, in the range 0.25–1.2 (see Methods, Table 2). The absorption lines are broad (with a mean linewidth $\Delta v_{abs}\approx400$ km s^{-1}) and three out of the five that were detected are blueshifted relative to the CH^+ emission-line centroid (v_{em}; Table 2). In the Eyelash galaxy, the CH^+ absorption covers the same velocity range as does the OH 119-μm absorption[20]. Three of the CH^+ emission lines are broader than 1,000 km s^{-1} (full-width at zero-intensity FWZI = 2,500 km s^{-1}), far broader than the known CO and H_2O lines of these galaxies[21–23] (Extended Data Table 1). Unlike the absorption lines, these broad emission lines are all centred within 30 km s^{-1} of the known redshift of the SMGs, and their width is independent of the star-formation rate (Tables 1 and 2).

We detect absorption in five out of the six targets observed. This high detection rate suggests that the absorbing gas has a quasi-isotropic distribution, a large covering fraction on the SMG dust continuum emission and is a feature that is common to the starburst phase. The lifetime of the absorbing medium is therefore comparable to that of the starburst phase $t_{SMG}\approx100$ Myr from SMG samples[2]. The low-density gas that is traced by CH^+ absorption cannot be confined within the starburst galaxies, because its thermal pressure is orders of magnitude below the high pressure in these $z\approx2$ galaxies[24]. We ascribe the absorption linewidths to turbulence (see Methods), with mean turbulent velocity $\overline{v}_{abs}=0.7\Delta v_{abs}$.

CH^+ column densities are derived from the absorption line profiles (see Methods, Table 2). The CH^+ molecules must form in the regions of dissipation of turbulence because, once formed, their lifetime is so short that they cannot be transported. Their abundance is inferred from the turbulent energy flux that sustains the number of observed CH^+ molecules (see Methods). This energy flux depends on the unknown radius r_{TR} of the turbulent reservoirs, being proportional to $\overline{v}^3_{abs}/r_{TR}$. Importantly, in the two targets with enough ancillary data on stellar and gas masses (the Eyelash[24] and SDP17b[25]), the mean turbulent velocities are equal to the escape velocities $v_{esc}(r)=(2GM_{tot}/r)^{1/2}$ at radii of $r=15.6$ kpc and $r=22.7$ kpc, respectively. Here G is the gravitational constant and M_{tot} is the sum of the stellar (M_*) and gas (M_{gas}) masses.

Table 1 | Properties of the lensed SMGs and CH^+ line and continuum fluxes

Name	z	μ	log[L_{FIR} ($L_\odot$)]	r_{SMG} (kpc)	SFR ($M_\odot$ yr^{-1})	$S_{1.2\,mm}$ (mJy)	S_{CH^+} (mJy)
Eyelash	2.3	37.5*	12.22 ± 0.07	0.3‡	285	38.15	5.4
G09v1.40	2.0	15.3 ± 3.5†	12.37 ± 0.09	0.41	404	30.12	7.4
SDP17b	2.3	6.2 ± 0.2	12.82 ± 0.05	0.72	1133	13.52	1.7
NAv1.56	2.3	9.79 ± 0.12	12.87 ± 0.05	0.76	1105	18.73	3.5
NAv1.144	2.2	4.16 ± 0.12	12.89 ± 0.08	0.84	1338	18.57	>3.8
SDP130	2.6	8.6 ± 0.4	12.33 ± 0.07	1.2	367	7.4	2.

The IAU full names that provide the galactic coordinates of the sources, as well as the full precision redshifts used, are given in Extended Data Table 1. The magnification μ and half-light size r_{SMG} are inferred from lens modelling of our ALMA data at rest-frame 360 μm (see Methods). The uncertainty on the half-light size is approximately 15%. The intrinsic far-infrared luminosity L_{FIR} is integrated over 40–120 μm (ref. 16), unlensed with our lens models. The star-formation rates (SFRs) are determined assuming a Salpeter initial mass function[16] and no contribution from active galactic nuclei; they are intended to illustrate only the differences among the galaxies. $S_{1.2\,mm}$ is the observed continuum flux of the sources. The observed peak CH^+ line emission flux S_{CH^+} is integrated over a solid angle defined by the contour level that is 0.05 times the peak continuum level. All uncertainties are 1σ root-mean-square (r.m.s.).
*Value taken from ref. 24.
†Value taken from ref. 16.
‡Size in the source plane of the brightest star-forming region (source X)[24].

[1]LERMA/LRA, Observatoire de Paris, PSL Research University, CNRS, Sorbonne Universités, UPMC Université Paris 06, Ecole normale supérieure, 75005 Paris, France. [2]European Southern Observatory, Karl-Schwarzschild-Strasse 2, 85748 Garching, Germany. [3]University of Michigan, Ann Arbor, Michigan, USA. [4]Institute for Astronomy, University of Edinburgh, Blackford Hill, Edinburgh EH9 3HJ, UK. [5]CEA/AIM, Saclay, France. [6]Cornell University, Cornell, New York, USA. [7]IAP, CNRS, Sorbonne Universités, UPMC Université Paris 06, 75014 Paris, France. [8]Max Planck Institute für Astronomie, Heidelberg, Germany.

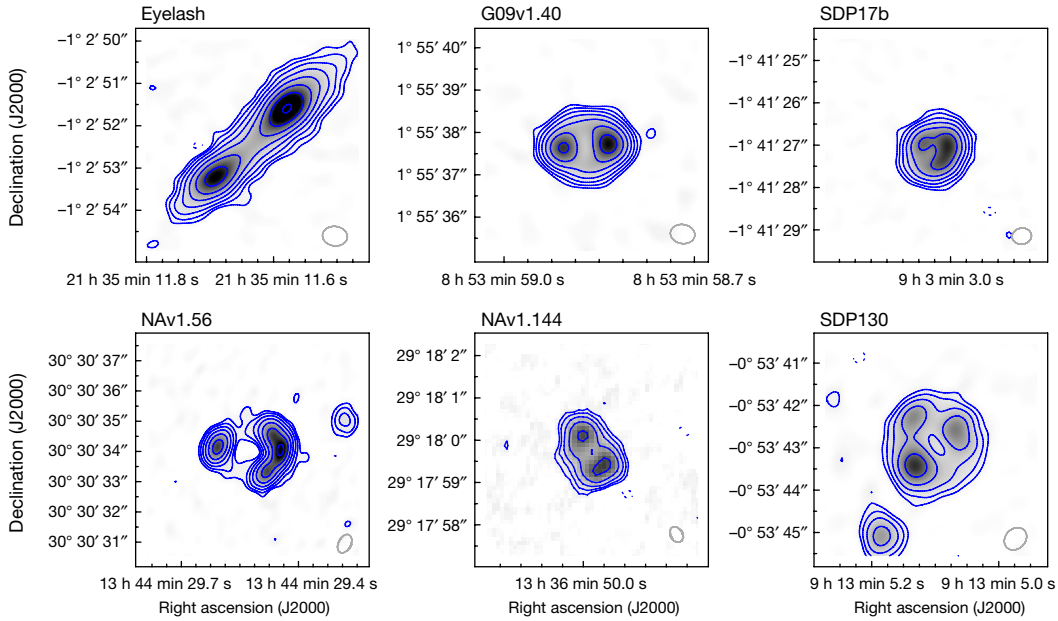

Figure 1 | Rest-frame 360-μm continuum images of our lensed targets. Solid contours are in steps of 3σ, showing $3\sigma \times 2^n$, $n = 0, 1, 2, \ldots$, and dashed contours are -3σ, where σ is the root-mean-square (r.m.s.) noise level (Table 1). The synthesized beam is shown in the bottom right corner (grey ellipse). In the Planck cosmology[30], 1 arcsec corresponds to 8.4 kpc at $z = 2.3$ (uncorrected for lensing magnification).

The key provision here is that the associated dynamical times, $t_{\rm dyn} = r/\bar{v}_{\rm abs}$=67 Myr and 46 Myr, respectively, are commensurate, whereas the stellar masses of these galaxies differ by a factor of 10. We therefore adopt $t_{\rm TR} \approx 50$ Myr as an approximate age of the observed turbulent reservoirs and $r_{\rm TR} = \bar{v}_{\rm abs} t_{\rm TR}$ for their radius. This radius is a lower limit because no dark matter contribution to the total mass $M_{\rm tot}$ was assumed. The estimated radii, in the range 10–20 kpc (Table 2), lead to CH^+ abundances that are similar to those in the Milky Way. The derived masses of the turbulent reservoirs, $M_{\rm TR}$, assuming a radial mean density distribution (see Methods), are in the range $(0.8–1.4) \times 10^{10} M_\odot$, where $M_\odot$ is the mass of the Sun (Table 2). These masses increase the gas mass fraction $M_{\rm gas}/M_{\rm tot}$ by only 10% in the Eyelash and SDP17b (see Methods). The kinetic luminosities of the turbulent reservoirs $L_{\rm TR} = M_{\rm TR} \bar{v}_{\rm abs}^2/(2t_{\rm TR})$ are in the range $(1.2–4.5) \times 10^9 L_\odot$, where $L_\odot$ is the luminosity of the Sun (Table 2).

The broad CH^+ emission lines trace gas denser than about 10^5 cm^{-3} with prodigious velocity dispersions. However, the CH^+ molecules cannot form in shocks faster than about 90 km s^{-1}, otherwise H_2 (which is required to form CH^+) would be dissociated[26]. Instead they must originate in countless lower velocity shocks that are sufficiently numerous not to be diluted. Irradiated magnetized shocks, propagating at $v_{\rm sh} \approx 40$ km s^{-1} in dense pre-shock gas, are the most efficient at producing CH^+ (see Methods). The CH^+ column densities of the shocked gas are high enough to emit lines that are much brighter than those detected, allowing for substantial beam dilution.

The CH^+ spectra provide considerable insight into the physics of these extreme star-forming systems. Although the sample size is small, the concomitance of the broad emission and deep absorption lines of CH^+ suggests that they trace coeval processes; that is, the dense shocks with high velocity dispersion and the dilute turbulent reservoirs are

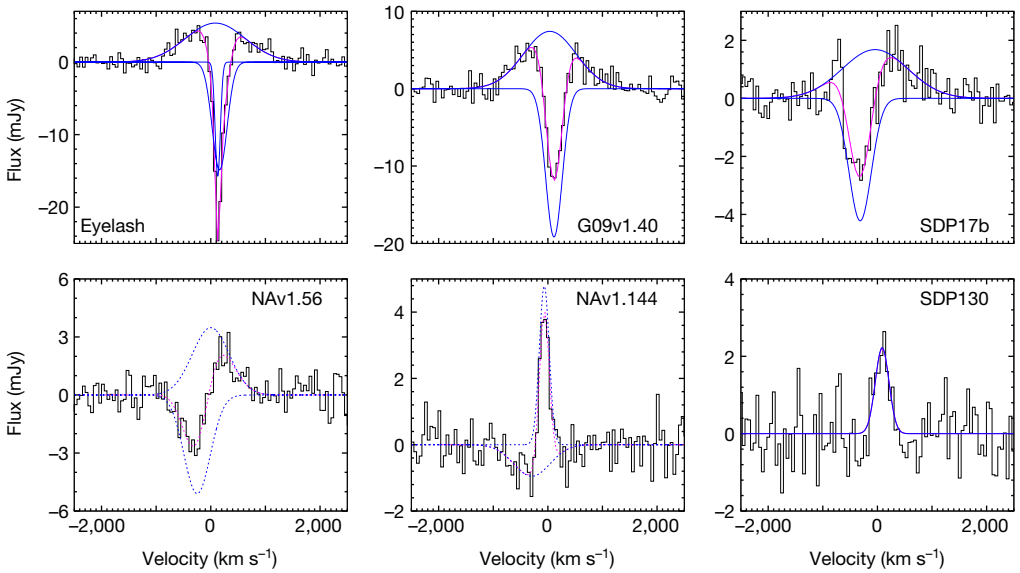

Figure 2 | CH^+ $J = 1–0$ spectra of our lensed targets. Continuum-subtracted spectra, integrated over the solid angle defined in Table 1. The pink curves show the final fits; the blue curves show the contributions of the emission (one Gaussian) and absorption (one or two Gaussians). The large velocity overlap of the absorption and emission in NAv1.56 and NAv1.144 makes the fits only indicative (dotted lines). The velocity scale is with respect to the accurate redshifts of Extended Data Table 1. The continuum was removed with a linear baseline to perform the fits.

Table 2 | Characteristics of the CH^+ line profiles and inferred properties of the turbulent reservoirs

Name	v_{em} (km s^{-1})	Δv_{em} (km s^{-1})	Δv_{abs} (km s^{-1})	v_{off} (km s^{-1})	τ_0	$N(CH^+)$ (10^{14} cm^{-2})	r_{TR} (kpc)	M_{TR} ($10^{10} M_\odot$)	L_{TR} ($10^9 L_\odot$)
Eyelash	30 ± 53	$1{,}301 \pm 112$	232 ± 40	143 ± 11	1.2	8.3	8	1.4	1.2
G09v1.40	28 ± 34	$1{,}124 \pm 87$	361 ± 24	111 ± 7	0.70	7.4	12	1.1	2.3
SDP17b	-21 ± 96	$1{,}394 \pm 157$	490 ± 53	-315 ± 28	0.33	4.7	17	0.9	3.4
NAv1.56*	0	>814	579	−249	0.29	4.9	20	0.8	4.5
NAv1.144*	0	>217	799	−227	0.25	6	–	–	–
SDP130	85 ± 21	248 ± 88	–	–	–				

The parameters v_{em}, Δv_{em}, Δv_{abs}, v_{off} and τ_0 are inferred from fits made simultaneously on the emission and absorption lines: Δv_{em} and Δv_{abs} are the full-width at half-maximum (FWHM) of the emission and absorption lines, respectively, v_{off} is the offset velocity of the absorption Gaussian, v_{em} is the emission line centroid velocity with respect to the systemic velocity of the galaxy as measured in CO, and τ_0 is the optical depth of the absorption peak (see Methods). $N(CH^+)$ is the average CH^+ column density in a solid angle subtended by the background source of radius r_{SMG} (see Methods). The radius, mass and kinetic luminosity of the turbulent reservoirs computed for $t_{TR} = 50$ Myr are denoted by r_{TR}, M_{TR} and L_{TR}, respectively (see Methods). Dashes indicate that the corresponding values cannot be derived.

*In these sources, the emission and absorption velocity coverages broadly overlap and the fits have been performed imposing $v_{em} = 0$. In NAv1.56, the convergence of the fit is poor; in NAv1.144, the strong residual emission is so narrow that the fit parameters are non-physical and have not been considered.

related. Yet, the disparity between the emission and absorption linewidths is striking. The emission linewidths (1,100–1,400 km s^{-1}) in the three sources in which they are well determined (the Eyelash, G09v1.40 and SDP17b) are very similar, whereas their star-formation rates span a factor of about 5. This finding suggests that these lines trace the fast thermal expansion of hot winds at similar temperatures T in the three sources. For outflow velocities of $v_{out} \approx \sqrt{3}\, c_s$, where

$$c_s \approx 500 \text{ km s}^{-1} \sqrt{\frac{T}{4 \times 10^7 \text{K}}}$$

is the sound velocity of the hot wind, the range of observed values ($v_{out} = 0.7 \Delta v_{em} \approx 700$–$1{,}000$ km s^{-1}) provides a range for the temperature of the hot wind of $T \approx (3\text{–}6) \times 10^7$ K. This high-velocity outflowing hot wind drives large-scale shocks in the dense outskirts of the starburst galaxies. Kinetic energy cascades within these shocks down to the velocity of the shocks that are able to form CH^+, in a process reminiscent of what is observed in the 35-kpc-long intergalactic shock in the group of galaxies known as Stephan's Quintet[27].

The outflowing wind eventually escapes from each galaxy, generating turbulence in its environment. It is this transition to turbulence that causes the outflow momentum to change from mostly outward to random and that allows the gas to be re-captured gravitationally. This is why the absorption linewidth in the Eyelash (which is ten times less massive than SDP17b) is smaller than in SDP17b. By preventing a fraction of the outflow from escaping from the large-scale galaxy potential well, turbulence makes this fraction available for further star formation[28]. Turbulence therefore mitigates the negative feedback of galactic winds on star formation, drawing out the starburst phase.

The CH^+ molecules that are seen in absorption are observed where they form, that is, in the turbulent dissipation sites of the 100-K dilute molecular phase; this suggests that the hot outflows also induce phase transitions in the galactic environments that could be the giant haloes of neutral hydrogen at 10^4 K that are detected in Lyman α (Lyα)[29] at high redshift. Importantly, the mass outflow rates that are required to sustain the kinetic luminosity L_{TR} of the turbulent reservoirs closely follow the star-formation rates (SFRs; see Methods):

$$\dot{M}_{out} = \frac{0.05\text{–}0.1}{\eta} \text{SFR} \left(\frac{v_{out}}{800 \text{ km s}^{-1}} \right)^{-2}$$

with $\eta < 1$ being the unknown efficiency of the energy transfer. This is so because the ratios L_{TR}/SFR are observed to be the same within a factor of 2 for all of the sources (Tables 1 and 2). If mass loss occurs at $v_{out} \approx 700$–$1{,}000$ km s^{-1}, as suggested by the broad emission lines, then the mass outflow rates are probably lower than the star-formation rates. Therefore, given their masses, the turbulent reservoirs that are drained by star formation cannot be fed by outflows only. They must be replenished over the lifetime of the starburst by other inflows, from tidal streams of ongoing major mergers or from cold stream accretion. The diffuse gas reservoirs result from the mixing of the gas that is ejected by the starburst-driven outflows, with gas present in the wider galactic environment.

By highlighting turbulent dissipation in cool molecular gas, CH^+ shows that mechanical energy, fed by gravity and galactic feedback, is largely stored in turbulence and eventually dissipated at low temperature rather than radiated away by hot gas. This turbulent energy storage is observed at two different stages of the feedback process: in the high-velocity-dispersion shocked dense gas close to the starburst galaxies, and very far from them, in the 10-kpc-scale massive reservoirs of low-density gas. Turbulence appears to be a key process in the triggering and subsequent regulation of star formation.

Online Content Methods, along with any additional Extended Data display items and Source Data, are available in the online version of the paper; references unique to these sections appear only in the online paper.

Received 26 January; accepted 21 June 2017.
Published online 14 August 2017.

1. Madau, P. & Dickinson, M. Cosmic star-formation history. *Annu. Rev. Astron. Astrophys.* **52,** 415–486 (2014).
2. Tacconi, L. J. *et al.* Submillimeter galaxies at $z \sim 2$: evidence for major mergers and constraints on lifetimes, IMF and CO-to-H_2 conversion factor. *Astrophys. J.* **680,** 246–262 (2008).
3. Carilli, C. L. & Walter, F. Cool gas in high-redshift galaxies. *Annu. Rev. Astron. Astrophys.* **51,** 105–161 (2013).
4. Veilleux, S., Cecil, G. & Bland-Hawthorn, J. Galactic winds. *Annu. Rev. Astron. Astrophys.* **43,** 769–826 (2005).
5. Förster Schreiber, N. M. *et al.* The SINS/zC-SINF survey of $z \sim 2$ galaxy kinematics: evidence for powerful active galactic nucleus-driven nuclear outflows in massive star-forming galaxies. *Astrophys. J.* **787,** 38 (2014).
6. Somerville, R. S. & Davé, R. Physical models of galaxy formation in a cosmological framework. *Annu. Rev. Astron. Astrophys.* **53,** 51–113 (2015).
7. Flower, D. & Pineau des Forêts, G. C-type shocks in the interstellar medium: profiles of CH^+ and CH absorption lines. *Mon. Not. R. Astron. Soc.* **297,** 1182–1188 (1998).
8. Lesaffre, P. *et al.* Low-velocity shocks: signatures of turbulent dissipation in diffuse irradiated gas. *Astron. Astrophys.* **550,** A106 (2013).
9. Godard, B., & Falgarone, E. & Pineau des Forêts, G. Chemical probes of turbulence in the diffuse medium: the TDR model. *Astron. Astrophys.* **570,** A27 (2014).
10. Godard, B. & Cernicharo, J. A complete model of CH^+ rotational excitation including radiative and chemical pumping processes. *Astron. Astrophys.* **550,** A8 (2013).
11. Falgarone, E. *et al.* Strong CH^+ $J = 1$–0 emission and absorption in DR21. *Astron. Astrophys.* **518,** L118 (2010).
12. Eales, S. *et al.* The Herschel ATLAS. *Publ. Astron. Soc. Pac.* **122,** 499–515 (2010).
13. Negrello, M. *et al.* The detection of a population of submillimeter-bright, strongly lensed galaxies. *Science* **330,** 800–804 (2010).
14. Bussmann, R. S. *et al.* Gravitational lens models based on submillimeter array imaging of *Herschel*-selected strongly lensed sub-millimeter galaxies at $z > 1.5$. *Astrophys. J.* **779,** 25 (2013).
15. Swinbank, A. M. *et al.* Intense star formation within resolved compact regions in a galaxy at $z = 2.3$. *Nature* **464,** 733–736 (2010).
16. Engel, H. *et al.* Most submillimeter galaxies are major mergers. *Astrophys. J.* **724,** 233–243 (2010).
17. Dekel, A. *et al.* Cold streams in early massive hot haloes as the main mode of galaxy formation. *Nature* **457,** 451–454 (2009).
18. Narayanan, D. *et al.* The formation of submillimetre-bright galaxies from gas infall over a billion years. *Nature* **525,** 496–499 (2015).
19. Schreiber, C. *et al.* The *Herschel* view of the dominant mode of galaxy growth from $z = 4$ to the present day. *Astron. Astrophys.* **575,** A74 (2015).

20. George, R. D. *et al. Herschel* reveals a molecular outflow in a $z = 2.3$ ULIRG. *Mon. Not. R. Astron. Soc.* **442,** 1877–1883 (2014).
21. Harris, A. I. *et al.* Blind detections of CO $J = 1$–0 in 11 H-ATLAS galaxies at $z = 2.1$–3.5 with the GBT/Zpectrometer. *Astrophys. J.* **752,** 152 (2012).
22. Lupu, R. E. *et al.* Measurements of CO redshifts with Z-Spec for lensed submillimeter galaxies discovered in the H-ATLAS survey. *Astrophys. J.* **757,** 135 (2012).
23. Omont, A. *et al.* H_2O emission in high-*z* ultra-luminous infrared galaxies. *Astron. Astrophys.* **551,** A115 (2013).
24. Swinbank, A. M. *et al.* The interstellar medium in distant star-forming galaxies: turbulent pressure, fragmentation, and cloud scaling relations in a dense gas disk at $z = 2.3$. *Astrophys. J.* **742,** 11 (2011).
25. Negrello, M. *et al.* Herschel-ATLAS: deep HST/WFC3 imaging of strongly lensed submillimetre galaxies. *Mon. Not. R. Astron. Soc.* **440,** 1999–2012 (2014).
26. Hollenbach, D. & McKee, C. F. Molecule formation and infrared emission in fast interstellar shocks. III. Results for *J* shocks in molecular clouds. *Astrophys. J.* **342,** 306–336 (1989).
27. Appleton, P. N. *et al.* Shock-enhanced C^+ emission and the detection of H_2O from the Stephan's Quintet group-wide shock using *Herschel*. *Astrophys. J.* **777,** 66 (2013).
28. Bouché, N. *et al.* The impact of cold gas accretion above a mass floor on galaxy scaling relations. *Astrophys. J.* **718,** 1001–1018 (2010).
29. Borisova, E. *et al.* Ubiquitous giant Lyα nebulae around the brightest quasars at $z \sim 3.5$ revealed with MUSE. *Astrophys. J.* **831,** 39 (2016).
30. Planck Collaboration. *Planck* 2013 results. XVI. Cosmological parameters. *Astron. Astrophys.* **571,** A16 (2014).

Acknowledgements ALMA is a partnership of ESO (representing its member states), NSF (USA) and NINS (Japan), together with NRC (Canada) and NSC and ASIAA (Taiwan), in cooperation with the Republic of Chile. The Joint ALMA Observatory is operated by ESO, AUI/NRAO and NAOJ. NRAO is a facility of the NSF operated under cooperative agreement by Associated Universities, Inc. R.J.I. acknowledges support from the ERC in the form of the Advanced Investigator Programme, 321302, COSMICISM. E.F. and B.G. acknowledge support from the national CNRS programme Physique et Chimie du Milieu Interstellaire (PCMI).

Author Contributions E.F., E.B., F.B. and D.E. conceived the initial scientific argument and wrote the ALMA proposal with B.G., M.A.Z., P.M.A., A.O. and R.S.B. M.A.Z. reduced the ALMA data. B.G. and E.F. analysed the spectra. B.G. provided the results of the shock models. R.J.I., I.O. and F.W. were invited to join the team at a later stage to provide the results of the lens models (I.O.) and to contribute to a year-long debate on the data interpretation. E.F. wrote the paper with contributions from all authors.

Author Information Reprints and permissions information is available at www.nature.com/reprints. The authors declare no competing financial interests. Readers are welcome to comment on the online version of the paper. Publisher's note: Springer Nature remains neutral with regard to jurisdictional claims in published maps and institutional affiliations. Correspondence and requests for materials should be addressed to E.F. (edith.falgarone@ens.fr).

METHODS

ALMA observations. The six targets were observed with ALMA in Cycle 2 as part of project 2013.1.00164.S (http://almascience.org/aq?project_code=2013.1.00164.S). The CH^+ (1–0) line ($\nu_{rest}=835.08$ GHz) at redshifts of $z\approx2.0$–2.6 is shifted into ALMA band 6 at frequencies of 230–270 GHz. The ALMA baseline correlator was configured to use three basebands in the upper sideband, so as to cover a maximum contiguous velocity range of approximately 5,000 km s^{-1} centred on the CH^+ line. The low-resolution Time Division Mode was used, which, using spectral averaging, provides 240 channels each of 7.812 MHz per baseband. This corresponds to a spectral resolution of 19 km s^{-1} after online Hanning smoothing. 32 to 34 antennas were used for these observations. A standard observing strategy was used, whereby a phase reference source was observed every 8 min. The total on-source time for the six sources combined was 195 min. Absolute flux calibration was obtained through the observation of Solar System objects and quasars with well-known flux values. The data calibration followed standard routines and was carried out using the CASA 4.4 (Common Astronomy Software Applications) package. Continuum images were made for each field using a 'robust' weighting scheme with a Briggs parameter of 0.5. All targets were sufficiently bright to perform one round of phase-only and one round of amplitude and phase self-calibration, which greatly improved the image quality and noise level. These self-calibrated datasets were subsequently used to construct data cubes centred around the redshifted CH^+ frequency, with a channel spacing of 50 km s^{-1}. The typical spatial resolution of the final data cubes is 0.5 arcsec, and the r.m.s. noise level is in the range 0.25–0.45 mJy per channel, depending on the data cube.

This paper makes use of the following ALMA data: ADS/JAO.ALMA#2013.1.00164.S.

Targets. *The Eyelash*. This three-image source, which is strongly lensed by a foreground cluster, has a combined amplification of 37.5 (ref. 24). High-resolution interferometry with the Sub-Millimeter Array (SMA) resolved the rest-frame 260-μm continuum emission in two sets of four clumps. The clumps have physical (source-plane) sizes of 100–300 pc in a region of 2 kpc within the background galaxy. The total gas mass inferred from CO is $M_{gas}\approx4\times10^{10}M_\odot$ and the stellar mass is $M_*\approx3\times10^{10}M_\odot$ (ref. 24), giving a gas mass fraction of $f_{gas}=M_{gas}/(M_*+M_{gas})\approx60\%$. The energy distribution of the CO spectral lines suggests that the Eyelash is a multiple component system with different conditions[31]. Low-density gas at low temperature is required to model the low-lying transitions of CO. The OH absorption line[20] is interpreted as an outflow that originated in the largest star-forming region of the galaxy.

The H-ATLAS sources. The redshift determination in G09v1.40 from the H_2O lines[32], $z=2.093$, is different from the centred value[16] of the CH^+ emission line. 880-μm SMA observation of the dust continuum shows two close components with a separation of about 1 arcsec along the east and west direction. The lensing model[16] gives $\mu=15.3\pm3.5$. The 10-m Keck telescope and the Spitzer space telescope images in the near- and mid-infrared, respectively, agree about a stellar component magnification of $\mu=11.4^{+0.9}_{-1}$ (ref. 33). For all of the other sources, the results of the lensing model applied to our ALMA data (Table 1) differ by 20% from those inferred from the SMA data[16], except for SDP130, for which the ALMA-inferred magnification is about four times that from SMA. NAv1.56 is a possible merger at a projected separation of 29 kpc (3.5 arcsec). In SDP17b, the total gas mass inferred from CO is $M_{gas}=5.9\times10^{10}M_\odot$ and the stellar mass is $M_*\approx2.4\times10^{11}M_\odot$ (ref. 25), so that the gas mass fraction is $f_{gas}\approx20\%$.

The IAU names of the targets, their redshifts and the characteristics of their CO and H_2O lines are given in Extended Data Table 1.

Exploitation of the CH^+ line profiles. CH^+ has such a highly endoenergic formation route via $C^+ + H_2$ ($E_{form}\approx0.4$ eV) that a specific chemistry activated by suprathermal processes is necessary[7–9]. Its fast destruction due to collisions with H and H_2 makes its lifetime extremely short, even in dilute gas. Being a light hydride with a high dipole moment, the critical density of its $J=1$–0 transition is approximately 10^7 cm^{-3}, about 10^4 times larger than that of CO $J=1$–0; so, in low-density gas, most molecules are in the ground state providing large $J=1$–0 line opacities. In absorption, CH^+ is therefore a tracer of dissipation of mechanical energy in a low-density gas ($n_H<10^2$ cm^{-3}). In contrast, in emission, the CH^+ $J=1$–0 line is a tracer of dense ($n_H>10^5$ cm^{-3}) ultraviolet-illuminated gas[12], such as ultraviolet-irradiated shocks, because, unlike most molecules, the abundance of CH^+ is enhanced in intense ultraviolet fields[10,11].

All of our targets are lensed starburst galaxies, with most likely different magnification for the dust continuum emission, the gas seen in absorption and that seen in emission. The angular and spectral resolution of our ALMA data provide information on the distributions of the absorption and the emission in velocity (Extended Data Fig. 1) and in space (Extended Data Figs 2 and 3). To interpret these data, differential modelling is warranted. However, the optical depth estimates of the absorption lines are not affected by differential lensing because the background dust emission and the absorbed emission experience the same lensing. We fitted the emission and absorption lines simultaneously, and evaluated the uncertainties on the parameters inferred (Table 2) using the bootstrap method to take into account the correlation between the parameters and the noise level of the data. The broad overlap between the absorption and emission velocity ranges makes the uncertainty on the absorption linewidth larger than 100% for NAv1.56. For NAv1.144, no solution with broad emission is found by the fitting procedure, although it is physically plausible.

The emission line luminosities—computed as

$$L_{CH^+}=\frac{1.04\times10^{-3}S_{CH^+}\Delta v_{em}\nu_{rest}D_L^2}{1+z}$$

where D_L is the luminosity distance (in Mpc; Extended Data Table 1), $S_{CH^+}\Delta v_{em}$ is the line-integrated flux (in Jy km s^{-1}) and $\nu_{rest}=835.07895$ GHz—are in the range $(2–7)\times10^8L_\odot$. The optical depth of the absorption line, computed at the velocity v_0 of the absorption peak, is derived from these fits:

$$\tau_0=-\ln\left[\frac{S_{abs}(v_0)}{S_{cont}+S_{em}(v_0)}\right]$$

where S_{cont}, S_{abs} and S_{em} are the continuum, absorption and emission fluxes respectively.

The CH^+ column densities are the average values in a solid angle subtended by the area (πr^2_{SMG}) of the background source, which is assumed to be uniformly covered by the absorbing screen:

$$N(CH^+)=3\times10^{12}\ \mathrm{cm^{-2}}\ \tau_0\left(\frac{\Delta v_{abs}}{1\ \mathrm{km\ s^{-1}}}\right)$$

where Δv_{abs} is the FWHM of the absorption line.

The formal errors on $N(CH^+)$ essentially follow the signal-to-noise ratio of the data. The velocity resolution is coarse and we cannot rule out the possibility that portions of the line might be saturated. The estimated values of $N(CH^+)$ could therefore be lower limits, so in Table 2 we provide them without a compiled error.

The turbulent framework. Since its discovery in the diffuse interstellar medium (ISM)[34], the puzzle raised by the large CH^+ abundances had focused on our solar neighbourhood because the line used was an electronic transition ($\lambda\approx0.4$ μm) detected in absorption against nearby stars. The rest frequency of CH^+ ($J=1$–0) falls in a domain of high atmospheric opacity, and the first observations of CH^+ (1–0) were achieved with the Herschel satellite. The line was detected in absorption against the dust continuum of remote Galactic star-forming regions with Herschel/HIFI[11,35,36] and in absorption or emission with Herschel/SPIRE[37]. The Herschel/HIFI data reveal the large opacity of the CH^+ (1–0) line in absorption in the Milky Way and show that the CH^+ absorption profiles differ considerably from those of other lines[36]. The Herschel/SPIRE detections in nearby starbursts[38–40] lack spectral resolution to definitely disentangle emission and absorption, but Arp 220 has a strong absorption line whereas Mrk 231 has the line in emission. A recent detection of the visible lines of CH^+ against a supernova in M82 reveals a highly turbulent component[41].

In the Milky Way, the CH^+ abundances observed in the diffuse molecular gas were found to scale with the turbulent energy transfer rate per unit volume, ε. The models of turbulent dissipation regions provide an expression for this scaling[9]. In a turbulent cascade, the dissipation rate per unit volume is on average equal to the energy transfer rate per unit volume in the cascade: $\varepsilon_l=\rho_l\bar{v}_l^2/(2\tau_l)$, where $\tau_l=l/\bar{v}_l$ is the dynamical time of scale l, and $\bar{v}_l$ and ρ_l are the mean velocity and mean mass density at that scale, respectively. It is this quantity,

$$\varepsilon_l=\frac{1}{2}\frac{\rho_l\bar{v}_l^3}{l}$$

that is observed to be uniform on average, albeit with a huge scatter, in the inner Galaxy[42] and that is found to be an invariant in numerical simulations of compressible turbulence[43]. This quantity is shortened into 'turbulent energy flux' in what follows, because it is a flux in the wavenumber space of the turbulent cascade.

The fraction of the turbulent energy flux required to sustain the observed number of CH^+ molecules in the volume $\pi r^2_{bg}L$ subtended by the background continuum source (radius r_{bg}) and the length of the line of sight L is $\alpha=\dot{E}_{CH^+}/\dot{E}_{turb}$, with

$$\dot{E}_{CH^+}=\frac{N(CH^+)\pi r^2_{bg}E_{form}}{t}$$

and

$$\dot{E}_{turb}=\bar{\varepsilon}\pi r^2_{bg}L$$

The turbulent energy flux $\bar{\varepsilon}$ is a large-scale average and the CH^+ lifetime is $t = 1\,\mathrm{yr} \times f_{H_2}^{-1}[n_H/(50\,\mathrm{cm^{-3}})]^{-1}$, where $f_{H_2} = 2n(H_2)/n_H$ is the H_2 fraction and n_H and $n(H_2)$ are the proton and the H_2 densities, respectively. As a result, the CH^+ opacity of absorption lines that provides $N(CH^+)$ is a direct measure of the turbulent energy flux in the medium. Introducing $N_{H,abs} = \bar{n}_H L$ (the total column density of gas of average density $\bar{n}_H$ sampled by the absorption), the observed abundance is $X(CH^+) = N(CH^+)/N_{H,abs}$ and therefore $\alpha = X(CH^+) \times (\bar{n}_H/\bar{\varepsilon}) \times (E_{form}/t)$. In the solar neighbourhood[9], the average values are $\langle X(CH^+)\rangle = 7.6 \times 10^{-9}$, $\bar{n}_H \approx 1\,\mathrm{cm^{-3}}$ and $\bar{\varepsilon} \approx 10^{-25}\,\mathrm{erg\,cm^{-3}\,s^{-1}}$, so that $\alpha = 7.7 \times 10^{-4} f_{H_2} n_{50}$, where $n_{50} = n_H/(50\,\mathrm{cm^{-3}})$ is the local gas density. Galactic observations of [C II] absorption and C I emission along the same background sources where CH^+ absorption is observed show that this gas is indeed the cold neutral medium (CNM)[44]. The average H_2 fraction in this low-density molecular gas is found to be $\overline{f}_{H_2} = 0.4$ from CH and HF absorption lines along the same sightlines[36], with a density probably in the range $n_H = 30$–$50\,\mathrm{cm^{-3}}$. The filling factor of the CNM in which CH^+ forms, $f_v = \bar{n}_H/n_H$, is much less than unity.

Determining the properties of the turbulent reservoir. We follow the same line of argument to study the turbulent gas around the SMGs. The turbulent approach is supported by the fact that the narrowest (broadest) absorption components have the smallest (largest) velocity offsets v_{off}; see Table 2. We also rely on a fundamental property of turbulence—that a pencil beam across a turbulent volume samples all of the velocities because of the velocity correlations—to relate the size of the turbulent reservoir to the mean turbulent velocity provided by the absorption linewidth. We assume a negligible contribution of rotation to the absorption linewidths (see Extended Data Fig. 1). The unknown CH^+ abundance is therefore an average value over the volume sampled by the absorption, in the same way as in the Milky Way. We again express that a fraction α of the turbulent energy flux

$$\dot{E}_{turb} = \frac{1}{2}\frac{M_{abs}\bar{v}_{abs}^3}{r_{TR}}$$

in the gas mass $M_{abs} = \mu_p m_H N_{H,abs} \pi r_{SMG}^2$ sampled by the absorption is sufficient to sustain the number of CH^+ molecules observed in absorption against the background continuum source of radius r_{SMG}, $\dot{E}_{CH^+} = N(CH^+)\,\pi r_{SMG}^2 E_{form}/t$. We thus obtain the relation between the radius of the turbulent reservoir and the CH^+ abundance:

$$r_{TR} X(CH^+) = \alpha \frac{\mu_p m_H}{2}\frac{t}{E_{form}}\bar{v}_{abs}^3$$

where the mean turbulent velocity is $\bar{v}_{abs} = 0.7\Delta v_{abs}$ and μ_p is the mean mass per particle. CH^+ abundances in the range $(0.8$–$5.2) \times 10^{-8}$ follow from the estimated values of r_{TR}, and hydrogen columns in the range 10^{23}–$9 \times 10^{21}\,\mathrm{cm^{-2}}$ are inferred. The mass of the turbulent reservoir is then computed by assuming mass conservation across the different shells, regardless of the global inward/outward or turbulent motions, so that the average density of the reservoir decreases with radius as $\bar{n}_H \propto r^{-2}$. As a result, the hydrogen column density at impact parameter b decreases as $N_H(b) \propto b^{-1}$ and the mass is $M_{TR} = 2\pi\mu m_H r_{TR} r_{SMG} N_{H,abs}$.

Introducing $\Delta v_{400} = \Delta v_{abs}/(400\,\mathrm{km\,s^{-1}})$ and $N_{14} = N(CH^+)/(10^{14}\,\mathrm{cm^{-2}})$ for the observed quantities, so that $N_{14}/\Delta v_{400} = 12\tau_0$, $X_8 = X(CH^+)/10^{-8}$ for the inferred abundances, $\alpha_3 = \alpha/10^{-3}$ and $t_{50} = t_{TR}/(50\,\mathrm{Myr})$ for the most probable age of the turbulent reservoirs, with $t_{TR} \approx t_{SMG}/2 \approx 50\,\mathrm{Myr}$, the radius and mass of the turbulent reservoirs are respectively

$$r_{TR} = 14.0\,\mathrm{kpc} \times \Delta v_{400} t_{50}$$

and

$$M_{TR} = 3.8 \times 10^{10} M_\odot \tau_0 t_{50}^2 r_{SMG,kpc}\left(f_{H_2}\frac{n_{50}}{\alpha_3}\right)$$

and the CH^+ abundance is

$$X_8 = \frac{2.5\Delta v_{400}^2 \alpha_3}{t_{50} f_{H_2} n_{50}}$$

A mean mass per particle of $\mu_p = 1.27$ is adopted. These expressions help to distinguish the dependence of the inferred sizes and masses on the observed quantities (Δv_{abs} and N_{14}) and free parameters (f_{H2}, n_{50} and α_3). The local gas density n_{50} and the H_2 fraction introduce some degeneracy. However, the range of possible values is limited. From the Galactic studies, $\overline{f}_{H_2} = 0.4$ and the gas densities of the CH^+-rich regions are in the range 30–$50\,\mathrm{cm^{-3}}$. All of the determinations are therefore within factors of a few. The CH^+ abundances are similar to the Galactic values, as would be expected if the CH^+ production rate were comparable to that in the Galaxy and the metallicities were similar to solar metallicities, as is observed[45] in star-forming galaxies at $z \approx 2$.

The kinetic luminosity is equal to the energy input rate that is needed to balance the dissipation of the kinetic energy $E_{turb} = M_{TR}\bar{v}_{abs}^2/2$ in a dynamical time $t_{TR} = r_{TR}/\bar{v}_{abs}$ or, with the appropriate units

$$L_{TR} = 2.6 \times 10^9 L_\odot \frac{M_{TR,10}\Delta v_{400}^2}{t_{50}}$$

where $M_{TR,10} = M_{TR}/(10^{10} M_\odot)$. The mass outflow rate at velocity v_{out} that is required to balance turbulent dissipation, $L_{TR} = \eta \dot{M}_{out} v_{out}^2/2$ (assuming an efficiency $\eta < 1$ of the energy transfer), is

$$\dot{M}_{out} \approx \frac{19}{\eta} M_\odot\ \mathrm{yr^{-1}} \frac{L_9}{v_{800}^2}$$

where $L_9 = L_{TR}/(10^9 L_\odot)$ and $v_{800} = v_{out}/(800\,\mathrm{km\,s^{-1}})$.

The turbulent reservoirs are more than ten times larger than the SMGs. Such kiloparsec-scale haloes of low-density gas, comprising a neutral diffuse molecular phase, have been invoked to interpret the low-lying OH absorption lines in Arp 220[46] and Na I D absorption lines[47] in ULIRGs, as well as CO (1–0) lines that are broader than CO (3–2) lines in distant SMGs[48]. Large kiloparsec-scale haloes of atomic hydrogen are being discovered in the Lyα line around high-redshift galaxies[29,49]. Last, the gas of the turbulent reservoirs is multiphasic because its average density, $\bar{n}_{TR} = N_{H,abs}/r_{TR} \approx 0.2$–$6\,\mathrm{cm^{-3}}$, is less than that of the CH^+-rich gas at $n_H \approx 30$–$50\,\mathrm{cm^{-3}}$, which fills only a low (<10%) fraction of the volume.

Models of irradiated shocks. A medium that is shocked at high velocity emits ultraviolet photons that interact with the pre-shock gas[26]. Depending on the shock velocity, this radiative precursor heats, dissociates (for $v_{sh} > 90\,\mathrm{km\,s^{-1}}$) or even ionizes (for $v_{sh} > 120\,\mathrm{km\,s^{-1}}$) the upstream medium, hence preventing the formation of molecular species. Therefore, although CH^+ emission has very broad line profiles, it is necessarily formed in shocks of much lower velocity. The extremely broad CH^+ emission lines trace the large velocity dispersion of lower-velocity shocks, as observed in the kiloparsec-scale shock of Stephan's Quintet[27,50].

The production of CH^+ in low-velocity interstellar shocks has been studied using the Paris–Durham shock code, a state-of-the-art model that was recently improved to take into account the basic physics of photo-dominated regions[8]. In these starbursts, ultraviolet illumination comes from star formation, with a possible contribution from the thermal emission of the optically thick accretion disks of active galactic nuclei (AGNs). Using observations of 22 AGNs[51], we estimate that the luminosity of a typical AGN with redshift $z > 1$ is comparable to that due to high-mass star formation, taking dilution within the starburst into account. We ran the code for several values of the pre-shock density (10^3–$10^6\,\mathrm{cm^{-3}}$), the ultraviolet radiation field (10^0–10^4 times the solar neighbourhood value) and the shock velocity (10–$80\,\mathrm{km\,s^{-1}}$), assuming a magnetic field of $2[n_H/(1\,\mathrm{cm^{-3}})]^{1/2}\,\mu\mathrm{G}$ and a visible extinction (that is, shielding from ultraviolet photons) of 1 mag.

We find that the critical velocity, above which stationary *C*-type shocks cannot propagate, strongly depends on the density and the radiation field. Below the critical value ($v_{sh} \approx 40\,\mathrm{km\,s^{-1}}$; that is, *C*-type shocks), the large abundance of H_2 and the ion-neutral decoupling are sufficient to produce column densities of CH^+ as large as about $10^{14}\,\mathrm{cm^{-2}}$ in the shock front, within timescales smaller than the expansion timescale of the gas. Above this critical value (that is, *J*-type shocks), the rapid and self-sustained collisional dissociation of H_2 prevents the immediate formation of CH^+ in the post-shock where H_2 reforms and the temperature is still high enough. Column densities of CH^+ as large as those of *C*-type shocks are obtained for a kinetic energy input that is five times larger, over distances 100 times larger and for timescales larger than the expansion timescale of the post-shock gas. We conclude that *J*-type shocks are far less efficient than *C*-type shocks at producing CH^+.

Large CH^+ column densities, up to $N(CH^+) \approx 10^{14}\,\mathrm{cm^{-2}}$ and spread over several kilometres per second per shock, are formed in $v_{sh} = 20\,\mathrm{km\,s^{-1}}$ *C*-type shocks propagating in dense pre-shock gas ($n_H \approx 10^4\,\mathrm{cm^{-3}}$). Lines as bright as 1 mJy per beam, estimated in the Large Velocity Gradient approximation[52], are obtained over a broad range of shock densities $\geq 10^5\,\mathrm{cm^{-3}}$ and gas temperatures ≥ 100 K. This result does not greatly depend on the gas density. The thickness of each shock is very small, about a few hundred astronomical units. The number of shocks in the beam is difficult to estimate because it depends on the actual geometry of the shock ensemble and its distribution in velocity. Corrected for lensing with the magnifications estimated for the continuum emission, the intrinsic CH^+ peak brightnesses are about 0.1 mJy per beam. Hence, millions of low-velocity shocks are required in the beam to reproduce the observed CH^+ (1–0) brightness spread smoothly over about $1{,}000\,\mathrm{km\,s^{-1}}$. The CH^+ (1–0) line opacity of individual shocks is less than unity; therefore, there is no limitation on the emitted line due to radiative transfer.

The lack of detection of CO (1–0) lines as broad as the CH^+ (1–0) lines in our targets (except NAv1.56) in which CO (1–0) has been observed (Extended Data Table 1) is due to the much larger emissivity of the CH^+ (1–0) transition compared to CO (1–0). The Einstein coefficients for spontaneous emission are $A_{10} = 6.4 \times 10^{-3}\ s^{-1}$ for CH^+ (1–0)[12] and $A_{10} = 7.4 \times 10^{-8}\ s^{-1}$ for CO (1–0). For an optically thin line, an upper limit for the integrated intensity of the *i*–*j* line is provided by $N_i A_{ij} h\nu_{ij}$, so the CO column density in the $J = 1$ level has to offset the huge ratio $A_{10}\nu_{10}(CH^+)/[A_{10}\nu_{10}(CO)] \approx 1.6 \times 10^6$. Therefore, as long as the column density of CO in the shocks does not exceed that of CH^+ by a factor of about 10^7, which is the case in the low-velocity *C*-type shocks, the CO (1–0) line remains very weak and probably below the detection level.

Data availability. This paper makes use of the following ALMA data: ADS/JAO.ALMA#2013.1.00164.S, available at http://almascience.org/aq?project_code=2013.1.00164.S and from the corresponding author on reasonable request.

31. Danielson, A. L. R. *et al.* The properties of the interstellar medium within a star-forming galaxy at $z = 2.3$. *Mon. Not. R. Astron. Soc.* **410,** 1687–1702 (2011).
32. Yang, C. *et al.* Submillimeter H_2O and H_2O^+ emission in lensed ultra-luminous infrared galaxies at $z \sim 2$–4. *Astron. Astrophys.* **595,** A80 (2016).
33. Calanog, J. A. *et al.* Lens models of *Herschel*-selected galaxies from high-resolution near-IR observations. *Astrophys. J.* **797,** 138 (2014).
34. Douglas, A. E. & Herzberg, G. *CH*$^+$ in interstellar space and in the laboratory. *Astrophys. J.* **94,** 381 (1941).
35. Falgarone, E. *et al.* CH^+ (1–0) and $^{13}CH^+$ (1–0) absorption lines in the direction of massive star-forming regions. *Astron. Astrophys.* **521,** L15 (2010).
36. Godard, B. *et al.* Comparative study of CH^+ and SH^+ absorption lines observed towards distant star-forming regions. *Astron. Astrophys.* **540,** A87 (2012).
37. Naylor, D. A. *et al.* First detection of the methylidyne cation (CH^+) fundamental rotational line with the *Herschel*/SPIRE FTS. *Astron. Astrophys.* **518,** L117 (2010).
38. van der Werf, P. P. *et al.* Black hole accretion and star formation as drivers of gas excitation and chemistry in Markarian 231. *Astron. Astrophys.* **518,** L42 (2010).
39. Spinoglio, L. *et al.* Submillimeter line spectrum of the seyfert galaxy NGC 1068 from the *Herschel*-SPIRE Fourier transform spectrometer. *Astrophys. J.* **758,** 108 (2012).
40. Rangwala, N. *et al.* Observations of Arp 220 using *Herschel*-SPIRE: an unprecedented view of the molecular gas in an extreme star formation environment. *Astrophys. J.* **743,** 94 (2011).
41. Ritchey, A. M. *et al.* Diffuse atomic and molecular gas in the interstellar medium of M82 toward SN 2014*J*. *Astrophys. J.* **799,** 197 (2015).
42. Hennebelle, P. & Falgarone, E. Turbulent molecular clouds. *Astron. Astrophys. Rev.* **20,** 55–113 (2012).
43. Kritsuk, A. G., Lee, C. T. & Norman, M. L. A supersonic turbulence origin of Larson's laws. *Mon. Not. R. Astron. Soc.* **436,** 3247–3261 (2013).
44. Gerin, M. *et al.* [C II] absorption and emission in the diffuse interstellar medium across the Galactic plane. *Astron. Astrophys.* **573,** A30 (2015).
45. Bothwell, M. S. *et al.* Molecular gas as the driver of fundamental galactic relations. *Mon. Not. R. Astron. Soc.* **455,** 1156–1170 (2016).
46. Gonzalez-Alfonso, E., Smith, H. A., Fischer, J. & Cernicharo, J. The far-infrared spectrum of Arp 220. *Astrophys. J.* **613,** 247–261 (2004).
47. Martin, C. Mapping large-scale gaseous outflows in ultraluminous galaxies with Keck II ESI spectra: variations in outflow velocity with galactic mass. *Astrophys. J.* **621,** 227–245 (2005).
48. Ivison, R. J. *et al.* Tracing the molecular gas in distant submillimetre galaxies via CO(1–0) imaging with the Expanded Very Large Array. *Mon. Not. R. Astron. Soc.* **412,** 1913–1925 (2011).
49. Wisotzki, L. *et al.* Extended Lyman α haloes around individual high-redshift galaxies revealed by MUSE. *Astron. Astrophys.* **587,** A98 (2016).
50. Guillard, P. *et al.* Turbulent molecular gas and star formation in the shocked intergalactic medium of Stephan's Quintet. *Astrophys. J.* **749,** 158 (2012).
51. Shull, J. M., Stevans, M. & Danforth, C. W. *HST*-COS observations of AGNs. I. Ultraviolet composite spectra of the ionizing continuum and emission lines. *Astrophys. J.* **752,** 162 (2012).
52. van der Tak, F. F. S. A computer program for fast non-LTE analysis of interstellar line spectra. *Astron. Astrophys.* **468,** 627–635 (2007).
53. Omont, A. *et al.* Observation of H_2O in a strongly lensed *Herschel*-ATLAS source at $z = 2.32011$. Astron. *Astrophys.* **530,** L3 (2011).

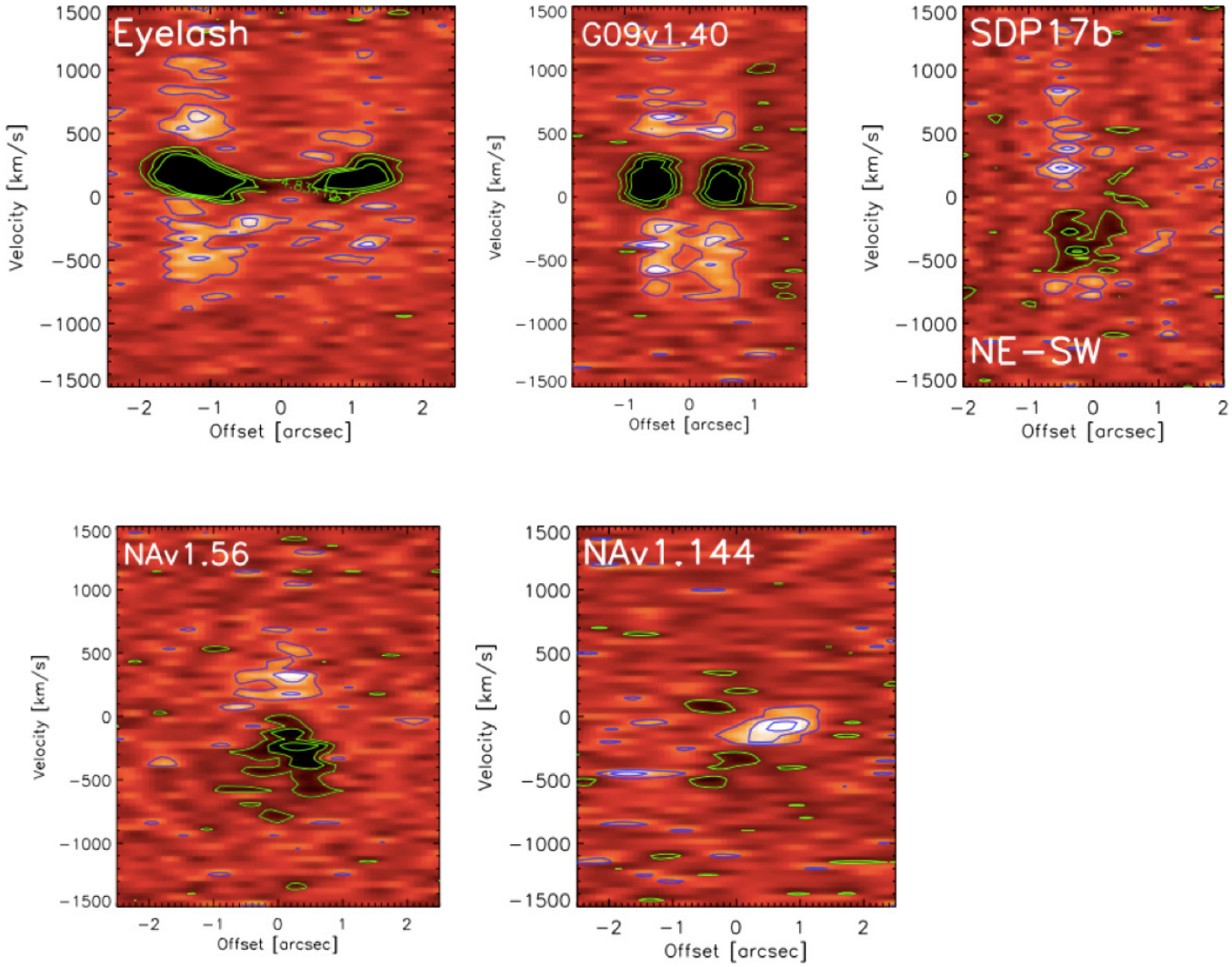

Extended Data Figure 1 | Position–velocity diagrams of CH^+ emission and absorption along selected cuts across the sources. The cuts are made along the east–west direction for G09v1.40, NAv1.56 and NAv1.144, along the long axis of the lensed images for the Eyelash, and along a northeast–southwest direction for SDP17b. CH^+ emission appears in white (blue contours) and absorption in black (green contours). The first contour level and steps are 2σ. A velocity gradient is seen in the absorption of the Eyelash that is two times smaller than that detected in CO (ref. 24).

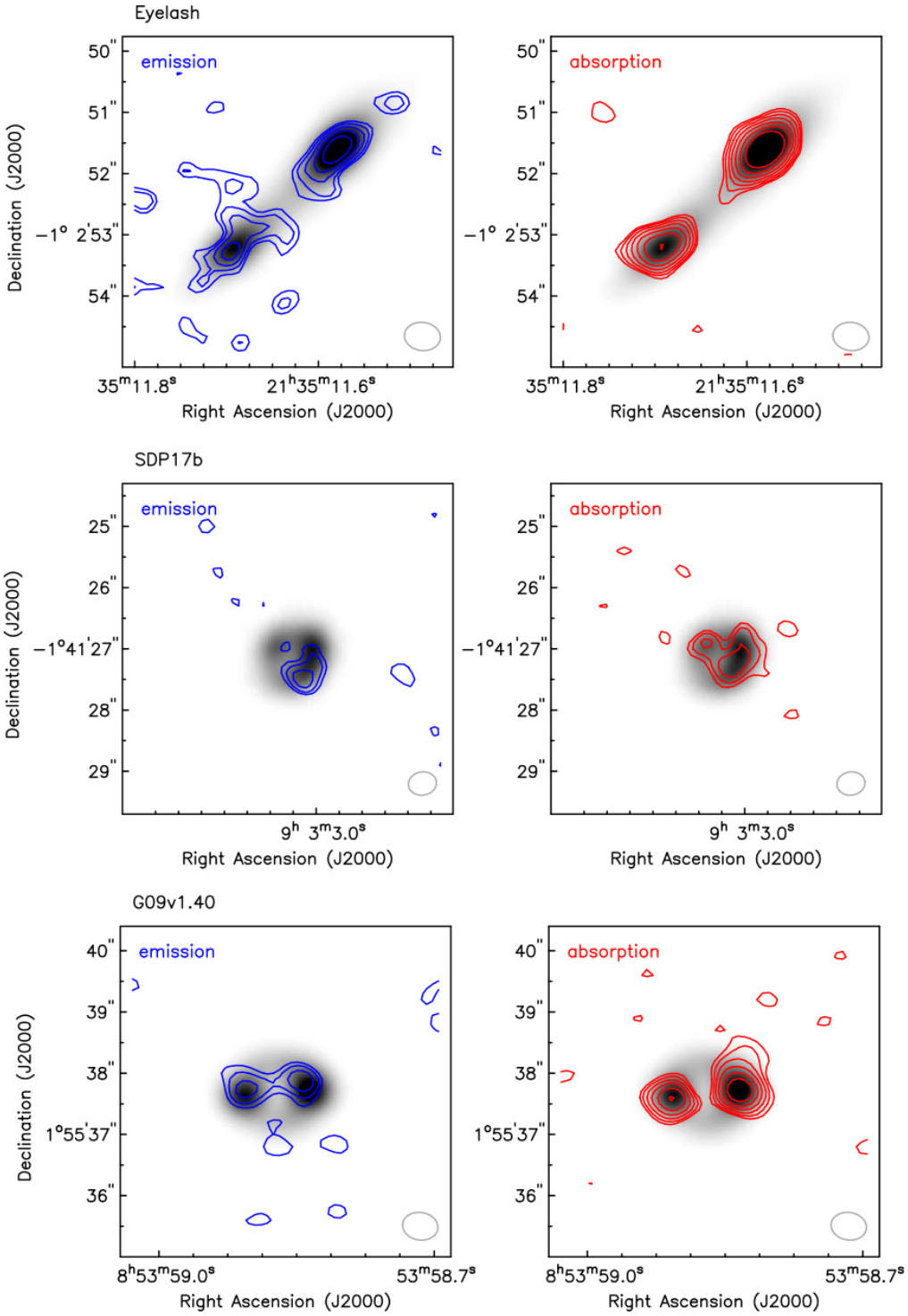

Extended Data Figure 2 | CH^+ emission and absorption overlaid on dust continuum emission for the Eyelash, SDP17b and G09v1.40. The integrated emission (blue contours) and absorption (red contours) of the CH^+ lines, with contour levels in steps of 2σ, are overlaid on continuum emission (grey scale). All of the images are lensed and so the differences between the distribution of dust continuum and CH^+ line emission are affected by differential lensing.

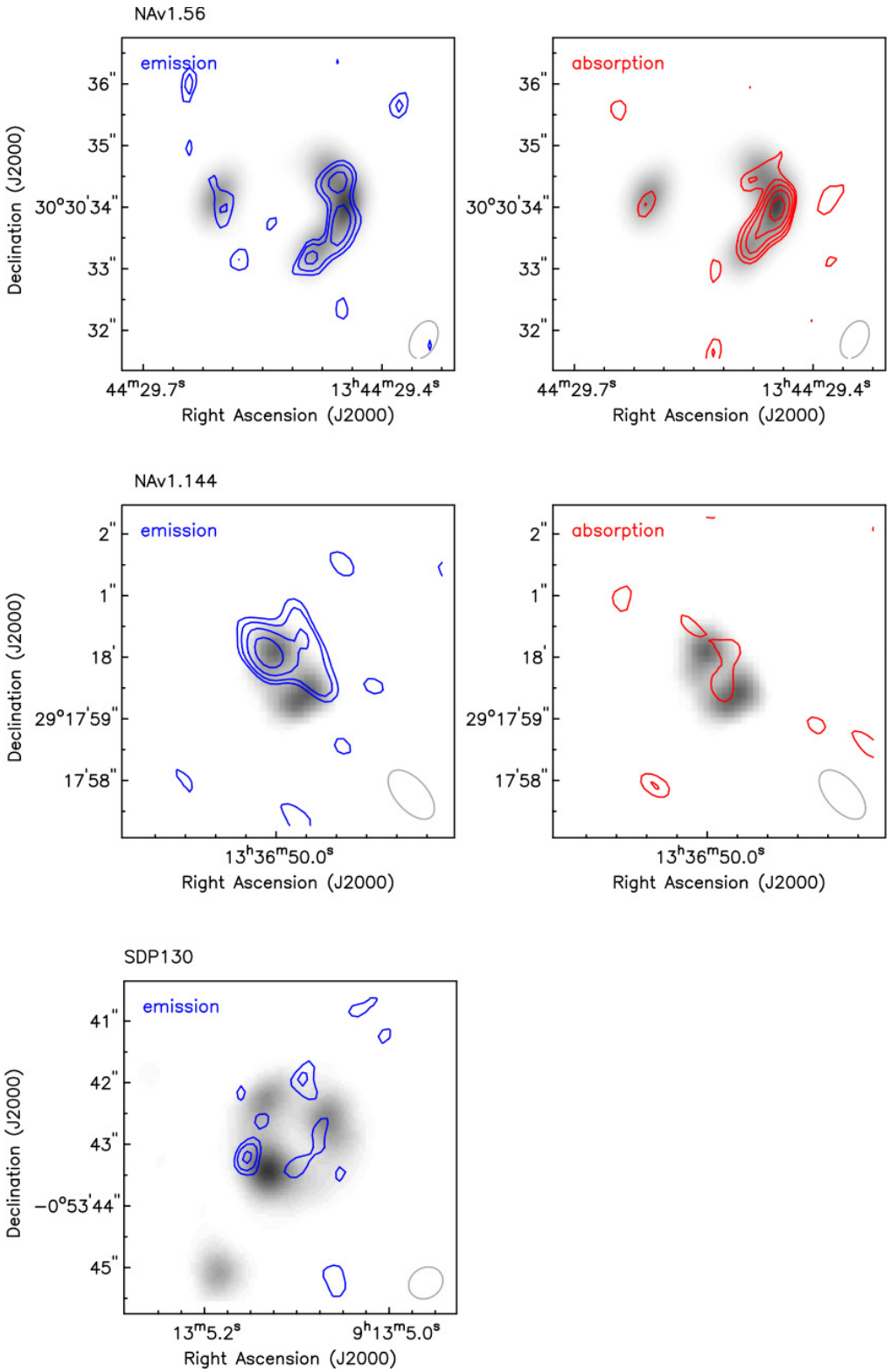

Extended Data Figure 3 | As in Extended Data Fig. 2, but for NAv1.56, NAv1.144 and SDP130. Only emission is detected for SDP130.

Extended Data Table 1 | Additional properties of the lensed SMGs

Name	IAU name	z	D_L [a] Gpc	CO line	S_{CO} [c] Jy km s^{-1}	Δv_{CO} km s^{-1}	Δv_{H_2O} km s^{-1}
Cosmic Eyelash	SMMJ2135-0102	2.3259	18.95	1-0	2.16±0.11	290± 30	
G09v1.40	J085358.9+015537[b]	2.0894	16.97	4-3	7.5±2.3	198 ± 51	277±14
SDP17b	J090302.9-014127 [b]	2.3051	18.95	1-0	0.9±0.1	320± 10	250±60
NAv1.56	J134429.4+303036 [b]	2.3010	18.95	1-0	1.1±0.1	1140±130	593±56
NAv1.144	J133649.9+291801 [b]	2.2024	17.95	1-0	0.9±0.1	220±20	200±50
SDP130	J091305.0-005343 [b]	2.6256	21.98	1-0	0.71±0.07	360±40	

The value of Δv_{H2O} for SDP17b is from ref. 53; those for NAv1.56 and NAv1.144 are from ref. 32.
[a]Luminosity distances D_L are computed for $H_0 = 67.3$ km s^{-1} Mpc^{-1}, $\Omega_M = 0.315$ and $\Omega_\Lambda = 0.685$ (ref. 30).
[b]H-ATLAS sources are from ref. 12 and redshift determinations from ref. 14.
[c]The CO (1–0) results for the H-ATLAS sources are from GBT/Zspec observations[21].